

## Article

# Smart Textile Flexible MnCo<sub>2</sub>O<sub>4</sub> Electrodes: Urea Surface Modification for Improved Electrochemical Functionality

Manesh A. Yewale <sup>1</sup>, Aviraj M. Teli <sup>2</sup>, Sonali A. Bektalkar <sup>2</sup>, Vineet Kumar <sup>1</sup> and Dong-Kil Shin <sup>1,\*</sup>

<sup>1</sup> School of Mechanical Engineering, Yeungnam University, Gyeongsan 38541, Republic of Korea; maneshphd@gmail.com (M.A.Y.); vineetfri@gmail.com (V.K.)

<sup>2</sup> Division of Electronics and Electrical Engineering, Dongguk University-Seoul, Seoul 04620, Republic of Korea; avteli.teli@gmail.com (A.M.T.); sonaliabektalkar@gmail.com (S.A.B.)

\* Correspondence: dkshin@yu.ac.kr

**Abstract:** Surface microstructure modification of metal oxides also improves the electrochemical performance of metal oxide nanoparticles. The present investigation demonstrates how varying the urea molar content during the hydrothermal process altered the surfaces of MnCo<sub>2</sub>O<sub>4</sub> nanoparticles. Successive increases of 0.1 M in urea concentration transformed the surface shape of MnCo<sub>2</sub>O<sub>4</sub> nanoparticles from flower-like to sheet-like microstructures. Excellent electrochemical performance of MnCo<sub>2</sub>O<sub>4</sub> nanoparticles was demonstrated in an aqueous 1 M KOH electrolyte. The improved MnCo<sub>2</sub>O<sub>4</sub> nanoparticles have been employed to develop an asymmetric supercapacitor (ASC). The ASC device exhibits an energy density of 13 Wh/kg at a power density of 553 W/kg and a specific capacitance of 29 F g<sup>-1</sup> at a current density of 4 mA/cm<sup>2</sup>. The MnCo<sub>2</sub>O<sub>4</sub> nanoparticle electrode demonstrates remarkable electrocatalytic activity in both HER and OER. The MnCo<sub>2</sub>O<sub>4</sub> electrode shows overpotential for HER and OER at 356 mV and 1.46 V, respectively. The Tafel slopes for HER and OER of the MnCo<sub>2</sub>O<sub>4</sub> electrode are 356 mV/dec and 187 mV/dec, respectively.

**Keywords:** MnCo<sub>2</sub>O<sub>4</sub> nanoparticles; supercapacitor; TEM; hydrothermal; asymmetric supercapacitor



**Citation:** Yewale, M.A.; Teli, A.M.; Bektalkar, S.A.; Kumar, V.; Shin, D.-K. Smart Textile Flexible MnCo<sub>2</sub>O<sub>4</sub> Electrodes: Urea Surface Modification for Improved Electrochemical Functionality. *Materials* **2024**, *17*, 1866. <https://doi.org/10.3390/ma17081866>

Academic Editor: Alessandro Dell'Era

Received: 7 March 2024

Revised: 11 April 2024

Accepted: 16 April 2024

Published: 18 April 2024



**Copyright:** © 2024 by the authors. Licensee MDPI, Basel, Switzerland. This article is an open access article distributed under the terms and conditions of the Creative Commons Attribution (CC BY) license (<https://creativecommons.org/licenses/by/4.0/>).

## 1. Introduction

The persistent consumption of petroleum and natural gas, propelled by an expanding global population, leads to natural resource deterioration and the emergence of serious energy shortages. Renewable energy sources paired with more effective technology for storing energy, represent an avenue for helping reduce pollution and improving energy challenges [1–7]. The accessibility to renewable energy sources, which are free of pollution, is essential for the development of the vehicle industry and human civilization as a whole. Electrocatalysis of the hydrogen evolution reaction (HER) and the oxygen evolution reaction (OER) are green energy alternatives that might be considered. Preparing nanoparticles for use in electrocatalysis can accomplish this. In order to solve future energy problems, HER use is crucial. As a result, hydrogen is going to be an essential component of sustainable energy systems in the future [8–10]. Electronic devices, whether powered by batteries or directly by sources such as electric cars, have seen enormous expansion, altering the landscape of fossil fuel-dependent gadgets [11–14]. Upcoming needs for energy indicate the necessity of high-energy and high-power sources. Nonetheless, while batteries are frequently used, they have a lower power density than supercapacitors. Supercapacitors gain more attention than batteries due to their inherent properties of rapid charge times, extended life, and flexibility. The flexibility of flexible supercapacitors, along with their simplicity of setup, makes them especially appropriate for a wide range of applications. The operational voltage window of hybrid solid-state supercapacitors has been expanded, resulting in higher energy density [15,16]. Supercapacitors have been separated into two varieties based on their charge storage mechanisms: pseudocapacitors and electric double-layer capacitors (EDLC). Metal oxides and chalcogenides primarily

demonstrate pseudocapacitor operation; however, carbon-based materials exhibit EDLC behavior. Transition metal oxides, including monometallic and bimetallic, have been getting an abundance of interest recently. Bimetallic oxides having spinel structures, such as  $AB_2O_4$  ( $B=Co$ ;  $A=Cu, Ni, Zn, Mn$ , etc.), have attracted substantial study focus for energy storage applications such as supercapacitors and electrolysis [17–20]. The synergy of two metals in the bimetallic oxides improves specific capacity, and the presence of numerous oxidation states accelerates faradic redox processes, which increases storage capacity even more [21–25]. Cobalt cation substitutes in bimetallic oxides alongside elements such as  $Zn, Ni, Cu$ , and  $Mn$ , offer benefits such as lower expenses, better conductivity of electricity, higher redox sites, and ecological friendliness. As a result of their greater valence state over  $Zn$  or  $Cu$ , manganese-based metal oxides have attracted quite a bit of attention [25,26].  $MnCo_2O_4$  exceeds monometal oxides such as  $MnO_2$  and  $Co_3O_4$  in electrochemical performance. Several methods to manufacture  $MnCo_2O_4$  nanoparticles with various microstructures (flowers, rods, and wires) in aqueous and non-aqueous solvents on favorable or flexible carbon cloth substrates have been reported. The electrochemical performance varies depending on the synthesis method, the surface microstructure, the solvent, and the substrate.

In the current article, we explore surface microstructure tailoring in the hydrothermal process by altering urea content. Hydrothermal approaches were used to synthesize  $MnCo_2O_4$  nanoparticles with urea concentrations that varied from 0.2 M to 0.5 M. Electrochemical performance was studied using electrodes made from flexible carbon fabric. Electrodes developed with a 0.3 M molar urea concentration in a 2 M potassium hydroxide electrolyte displayed remarkable electrochemical performance. Surface microstructure tweaking resulted in compelling variations in electrode performance, with nanowires linking to larger active sites and boosting energy storage capacity and electrocatalytic performance of the electrode. Electrodes and devices made from 0.3 M nanoparticles exhibited remarkable specific capacitance, energy density, power density and electrocatalytic performance.

## 2. Experimental

The hydrothermal method was used to synthesize the  $MnCo_2O_4$  nanoparticles. The following solutions were prepared by dissolving the following in 40 mL of deionized water: 0.1 M  $Mn(NO_3)_2 \cdot 6H_2O$ , 0.2 M  $Co(NO_3)_2 \cdot 6H_2O$ , and 0.2 M  $NH_2CONH_2$ . After 30 min of stirring, the solution was considered homogenous. After pouring the entire solution into a 100 mL sealed Teflon hydrothermal liner, it was put in a stainless-steel reactor. After being sealed, the reactor was placed in the oven. The hydrothermal process continued for nine hours at a constant temperature of 120 °C. The hydrothermal reactor was allowed to cool down to room temperature naturally once the reaction was finished. After the hydrothermal reaction was complete, the product was filtered through filter paper after several rinses with water and ethanol. After filtering, the precipitate was transferred in a Petri dish and left to dry overnight at 60 °C in the oven. The dried product was subsequently placed in a crucible and subjected to an annealing process at 400 °C for a duration of four hours to produce  $MnCo_2O_4$  nanoparticles. The  $MnCo_2O_4$  nanoparticles were named MCO-0.2 molar urea (MU) after cooling to room temperature following the annealing procedure. The MCO-0.3 MU, MCO-0.4 MU, and MCO-0.5 MU  $MnCo_2O_4$  nanoparticles were synthesized using the same procedure, by tuning urea concentrations to 0.3 M, 0.4 M, and 0.5 M, respectively. All sections of the article, including characterization, findings, and explanations, utilized the same terminology. Subsequent research and analysis made use of each sample.

### 2.1. Material Characterization

The specimens underwent crystallographic examination using X-ray diffraction (XRD) with PAN analytical equipment, employing  $Cu-K\alpha$  radiation. The oxidation states of the surface elements were determined using X-ray photoelectron spectroscopy (XPS) with K-alpha equipment from Thermo Scientific, Oxford, UK. Surface morphology and energy dispersive spectroscopic (EDS) analysis were conducted using a HITACHI Ltd. Tokyo,

Japan S-4800 field-emission scanning electron microscope (FE-SEM). Electrochemical data were acquired using a potentiostat (WonAtech, Zive SP-5, Seoul, Republic of Korea). A Tecnai F21 high-resolution transmission electron microscope (HRTEM) from FEI Company (Hillsboro, OR, USA) was used for a more comprehensive analysis of surface morphology and element mapping.

## 2.2. Electrode Preparation

Conducting stability tests, electrochemical impedance spectroscopy (EIS), cyclic voltammetry (CV), and galvanostatic charge-discharge (GCD) studies, the  $\text{MnCo}_2\text{O}_4$  nanoparticles were electrochemically studied at the Wonatech (SP-5) workstation. The carbon cloth (CC) electrodes measuring  $1 \times 2 \text{ cm}^2$  were used to prepare the electrodes. In NMP solvent,  $\text{MnCo}_2\text{O}_4$  nanoparticles, PVDF, and carbon black were mixed in a weight percentage ratio of 80:10:10. Next, a  $1 \times 1 \text{ cm}^2$  surface area CC was used to drop cast the prepared solution. In order to prepare the electrodes for further electrochemical investigations, they were oven-dried overnight at 60 degrees Celsius. The asymmetric supercapacitors were assembled using two electrodes: one made of optimized  $\text{MnCo}_2\text{O}_4$  and the other of activated carbon (YEC-8A). Activated carbon electrodes are made in an identical way as  $\text{MnCo}_2\text{O}_4$  electrodes, but instead of employing nanoparticles of  $\text{MnCo}_2\text{O}_4$ , activated carbon was employed.

## 3. Result and Discussion

### 3.1. X-ray Diffraction and X-ray Photoelectron Spectroscopy (XPS) Analysis

The analysis of XRD was employed to evaluate the structural phases and structure of the  $\text{MnCo}_2\text{O}_4$  nanoparticles. Figure 1 demonstrates the XRD spectra of  $\text{MnCo}_2\text{O}_4$  nanoparticles synthesized by various urea molar concentrations that vary between 0.2 to 0.5 M. The spectra reveal slight variations in peak intensity and sharpness. With rising urea molar concentrations, the peak intensity associated to the (400) plane diminishes. The nanoparticle XRD spectrum at 0.3 M concentration appears sharper than the other XRD spectra. Peaks can be recognized in all the XRD results at 18.77, 35.82, 43.66, 58.53, and 63.66, which correspond to (111), (311), (400), (511), and (440), respectively. These peaks are completely comparable to JCDPS card 00-001-1130, displaying the cubic phase growth of  $\text{MnCo}_2\text{O}_4$  nanoparticles with lattice parameters of 8.20Å. The X-ray photoelectron spectroscopy (XPS) details were used to study the  $\text{MnCo}_2\text{O}_4$  nanoparticles' oxidation state and composition. Figure 2a displays the XPS spectra obtained from the survey scan of the MCO-0.3 MU nanoparticle. The spectra illustrate that the prepared sample incorporates oxygen, manganese, and cobalt. Additionally, Figure 2b displays the Mn2p's high-resolution spectra. The convolution and deconvolution of the Mn2p spectra revealed two prominent peaks at 642.13 eV and 653.74 eV, respectively, which correspond to the Mn 2p<sub>3/2</sub> and Mn 2p<sub>1/2</sub> oxidation states. The occurrence of the Mn<sup>3+</sup> state appears by the peaks at 641.90 eV and 653.58 eV, whereas the existence of the Mn<sup>2+</sup> state is shown by the peaks at 644.02 eV and 654.95 eV, respectively [27]. Figure 2c displays the four-peak fitted convolution and deconvolution XPS spectra of the Co2p. It is also proposed to attribute peaks at 779.90 eV and 794.85 eV to Co<sup>3+</sup>, and peaks at 781.41 eV and 796.42 eV to Co<sup>2+</sup>. It is Co2p that appears as the satellite peak at 784.73 eV and 804.24 eV [28–30]. Three peaks at 529.93, 530.23, and 531.52 corresponding to Mn-O, C-O, and C=O bonds, respectively, are depicted in Figure 2d as the O1s' high-resolution spectra [28]. The results showed considerable matching with the XRD and EDS spectra and the XPS data, indicating that  $\text{MnCo}_2\text{O}_4$  nanoparticles had been formed.

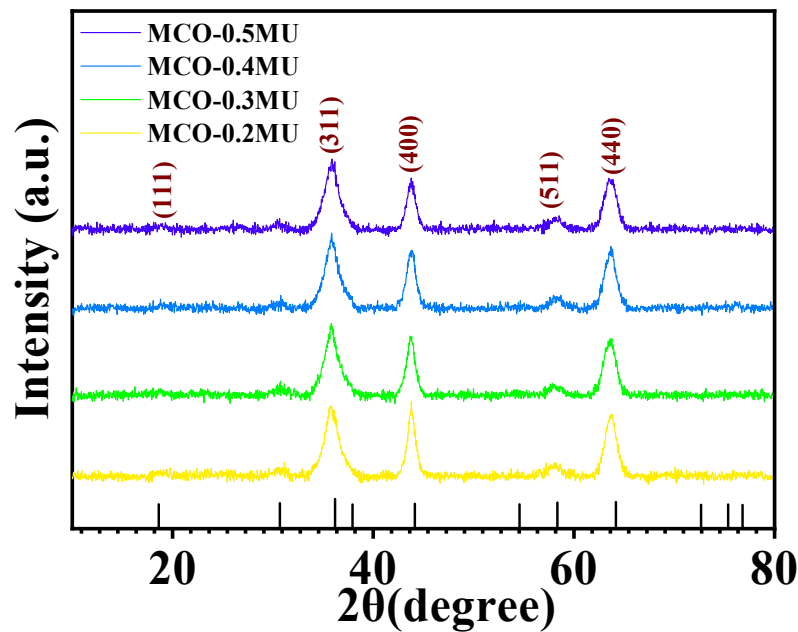


Figure 1. XRD spectra of  $\text{MnCo}_2\text{O}_4$  nanoparticles prepared at different molar concentration of urea.

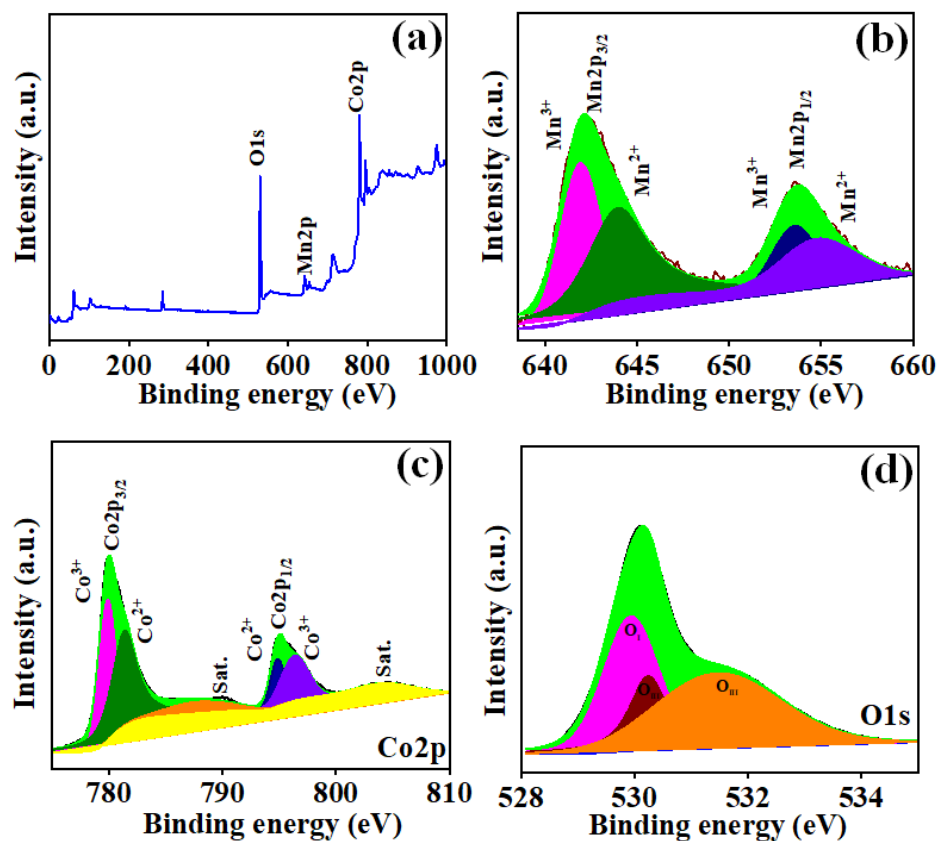


Figure 2. XPS spectra of MCO-0.3 MU (a) survey spectrum, (b), Mn2p, (c) Co2p and (d) O1s.

### 3.2. Morphological Analysis

The surface morphology of nanomaterials has an important effect on their electrochemical activity. The surface microstructure of the nanoparticles was examined using field-scanning electron microscopy (FESEM). Figure 3 depicts a FESEM micrograph of  $\text{MnCo}_2\text{O}_4$  nanoparticles synthesized using various urea concentrations in molar quantities and acquired at various magnifications. Figure 3(a1–a3) depicts a  $\text{MnCo}_2\text{O}_4$  nanoparticle

produced at a urea concentration of 0.2 M. The FESEM micrograph shows the beginnings of the growth of  $\text{MnCo}_2\text{O}_4$  nanoparticles with a flower-like shape, as well as the formation of the flower's petals. The petals of the  $\text{MnCo}_2\text{O}_4$  nanoparticles join together at the flower base and begin to expand in every direction, indicating the earliest flower's growth. A few of the petals combine jointly, providing a compact flower-like shape, and the influence on the electrode's electrochemical performance was observed. The compactness of the petals may make the insertion and extension of ions challenging, delivering a small impediment during the charging and discharging process, resulting in limited charge storage capacity of the electrode. The surface microstructure of the nanoparticles demonstrated the tuning of the floral structure alteration as the molar concentration of urea was set to 0.3 M. The development of the nanoparticles is accelerated at 0.3 M molar concentrations of urea, and distinct petals of the flower are visible. The flower's petals are fully opened from the free end side, allowing free space between each petal, and each petal resembles a wire-like structure, as observed in Figure 3(b1–b3). The ends of a few petals are attached from the free end together in the FESEM micrograph, and the bottom is likewise already joined with free spacing between the petals. All of these clumped petal structures combine to form a flower-like shape with open space between each petal. The effect of free space and the connecting of the tip of the petal on electrochemical performance in energy storage capacity has been identified. The free space enables effortless access for ions during charging and discharging, as revealed by a longer discharge time for the MCO-0.3 MU electrode in GCD as well as reduced series resistance and charge transfer resistance in the EIS study. At a 0.4 M urea concentration, vital modifications to the surface were detected. Figure 3(c1–c3) depicts a FESEM micrograph of  $\text{MnCo}_2\text{O}_4$  nanoparticles generated at 0.4 M urea concentration, revealing their modification from a flower-like morphology to a sheet-like structure. The petals of the flower in 0.3 M urea concentration clumped together laterally and began to overlap, resulting in the sheet-like morphology shown in the FESEM micrographs. As sheet making begins, barely any top and bottom surfaces are accessible for electrolyte and electrode interaction, and the surface microstructure tailoring results in electrochemical performance. Figure 3(d1–d3) depicts a FESEM micrograph of  $\text{MnCo}_2\text{O}_4$  nanoparticles with a consistent sheet-like surface shape at 0.5 M urea concentration. With urea concentration variations, the flower-like surface microstructure is entirely lost, transforming it into a sheet-like microstructure. The surface morphology adjustment also affects the electrode's electrochemical performance. As a whole, the petal-like microstructure demonstrates a flower-like shape with free petal-like structures at 0.3 M urea concentration, exhibiting better electrochemical performance, possibly due to the open space for interaction between the electrode and electrolyte. EDS analysis was used to figure out the elemental composition of the produced nanoparticles. Figure 4a–d depicts the EDS spectra of all  $\text{MnCo}_2\text{O}_4$  nanoparticles prepared at various urea molar concentrations. The presence of cobalt, manganese, and oxygen is indicated by prominent peaks in all EDS spectra. All spectra reveal  $\text{MnCo}_2\text{O}_4$  nanoparticle stoichiometry, which is well-matched with XRD data, indicating the phase development of the  $\text{MnCo}_2\text{O}_4$  nanoparticles. In addition, transmission electron microscopy (TEM) was employed to look into the surface microstructure of  $\text{MnCo}_2\text{O}_4$  nanoparticles synthesized at 0.3 M urea concentration. Figure 5 shows a TEM micrograph of the MCO-0.3 MU nanoparticle at various magnifications. Figure 5a–c demonstrates a TEM micrograph at magnifications, demonstrating the clearly visible growth of the flower-like structure by the petal structure resembling a wire-like microstructure. All of the nanowires are clumped together, producing a petal-like shape with some open space in between. Each nanowire is made up of small nanoparticles growing vertically to form a wire-like structure, as seen in the Figure 5c. These wires link together laterally, offering a petal-like structure with free spacing between the wire and tiny nanoparticles, which is more advantageous for the extraction of the electrolyte and electrode during charging and discharging via ion insertion and extraction. Perhaps as a result of this space, the electrode produced with MCO-0.3 MU nanoparticles exhibits remarkable electrochemical performance and the highest energy storage capacity. Figure 5d also depicts the MCO-0.3 MU

nanoparticle's selected area electron diffraction (SAED) pattern, which demonstrates a ring-like pattern, showing that the nanoparticles are polycrystalline in nature. The SAED results confirm the XRD outcomes, pointing to the polycrystalline nature of  $\text{MnCo}_2\text{O}_4$  nanoparticles. EDS analysis was used for further study of the constituent elements of the MCO-0.3 MU nanoparticle. The EDS spectra of MCO-0.3 MU nanoparticles appear in Figure 5e, illustrating the existence of cobalt, manganese, and oxygen. The EDS data correlate well with the XRD stoichiometry and phase of the nanoparticle.

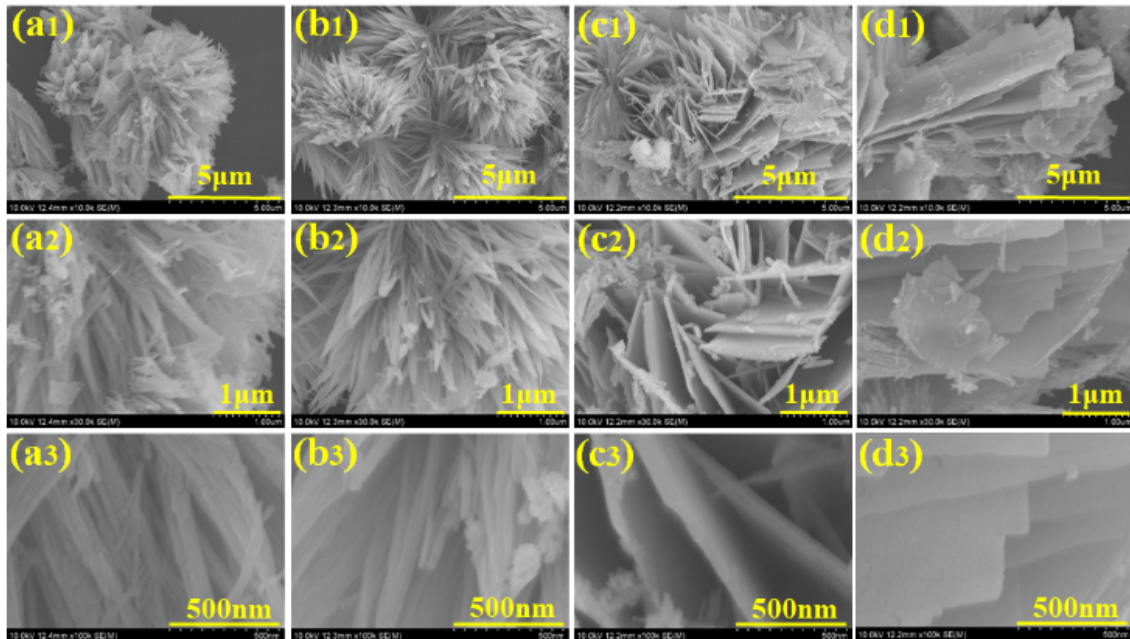


**Figure 3.** FESEM micrograph of  $\text{MnCo}_2\text{O}_4$  nanoparticles at different magnifications, MCO-0.2 MU (a1–a3), MCO-0.3 MU (b1–b3), MCO-0.4 MU (c1–c3), MCO-0.5 MU (d1–d3).

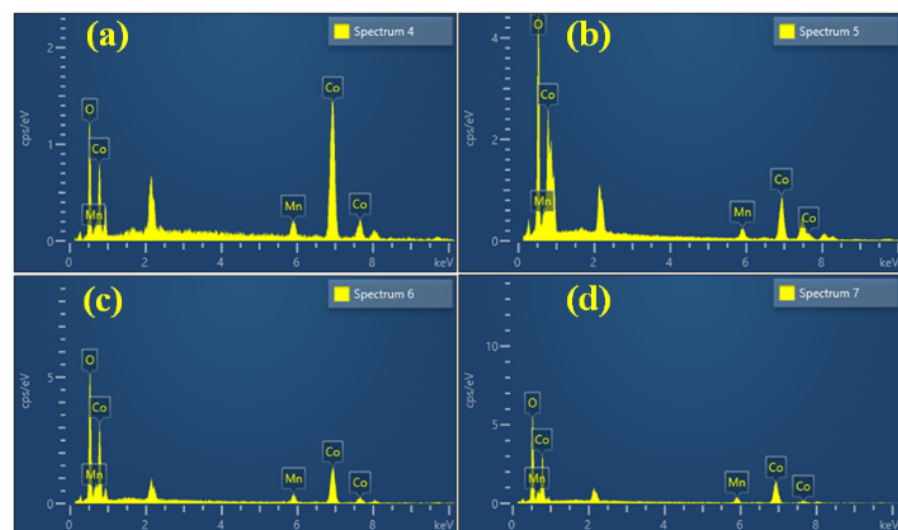


**Figure 4.** EDS spectra of  $\text{MnCo}_2\text{O}_4$  nanoparticles, MCO-0.2 MU (a), MCO-0.3 MU (b), MCO-0.4 MU (c), MCO-0.5 MU (d).

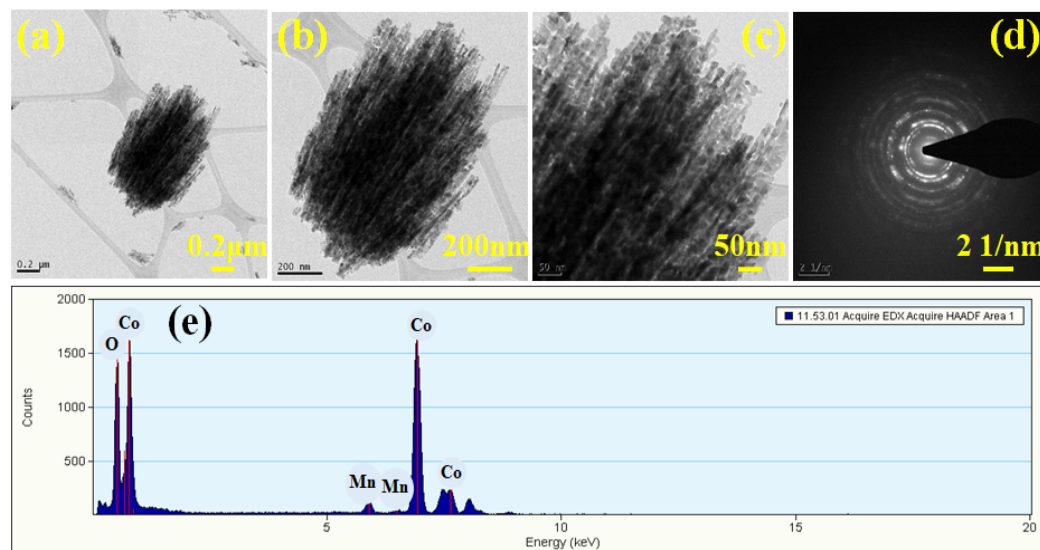


**Figure 5.** TEM micrograph at different magnifications (a–c), SAED pattern (d), EDS spectra (e) of MnCo<sub>2</sub>O<sub>4</sub> nanoparticles (MCO-0.3 MU).

### 3.3. Electrochemical Performance

The synthesized MnCo<sub>2</sub>O<sub>4</sub> nanoparticles were electrochemically studied using cyclic voltammetry (CV), galvanostatic charge-discharge (GCD), and electrochemical impedance spectroscopy (EIS). The electrochemical measurements have been carried out using aqueous 2 M KOH electrolyte. Figure 6 examines the comparative CV profiles of all electrodes in the potential range of 0.0–0.6 V. The findings show that the urea concentration substantially influences the electrode's electrochemical performance. The MCO-0.3 MU electrode has a greater area behind the CV profile than the other electrodes shown in the comparative CV profile depicted in as detailed in coming section. The surface architecture of the MCO-0.3 MU nanoparticles could be contributing to the larger area under the curve. The FESEM details suggest a flower-like form of petals with a nanowire structure and microscopic nanowires made up of tiny nanoparticles, as found in TEM examination. During the charging and discharging processes, these small nanoparticles provide accessible surface space for electrode-electrolyte interaction. The floral structure, with nanowire shape and empty spaces, benefits ion interaction, resulting in a greater area under the CV profile for the MCO-0.3 MU electrode when compared to the other electrodes. Figure 6a demonstrating CV profiles at various scan rates shows that the area beneath the CV profile increases as the scan rate increases, demonstrating that the electrode is reversible. With expanding scan rates, the oxidation and reduction peaks shift away from the formal potential, resulting in a drop in peak intensity. The CV profile also shows that the area under the CV profile for MCO-0.3 MU is bigger than the area under the CV profile for the other electrodes. In addition, the kinetics of the electrode was examined by looking at the *b* values. The *b* value is the slope of the  $\log(i_p)$  vs.  $\log(v)$ , as calculated from Equation (1) and Figure 7a,e for all electrode materials. According to the *b* value analysis, the charge storage mechanism is either diffusive (0.5) or capacitive (1.0) [31–33]. The computed *b* values for all electrodes fall between 0.47 and 0.62, suggesting a combination of both processes.

$$\log(i_p) = \log(a) + b \cdot \log(v) \quad (1)$$

$$i_p = k_c v + k_d v^{1/2} \quad (2)$$

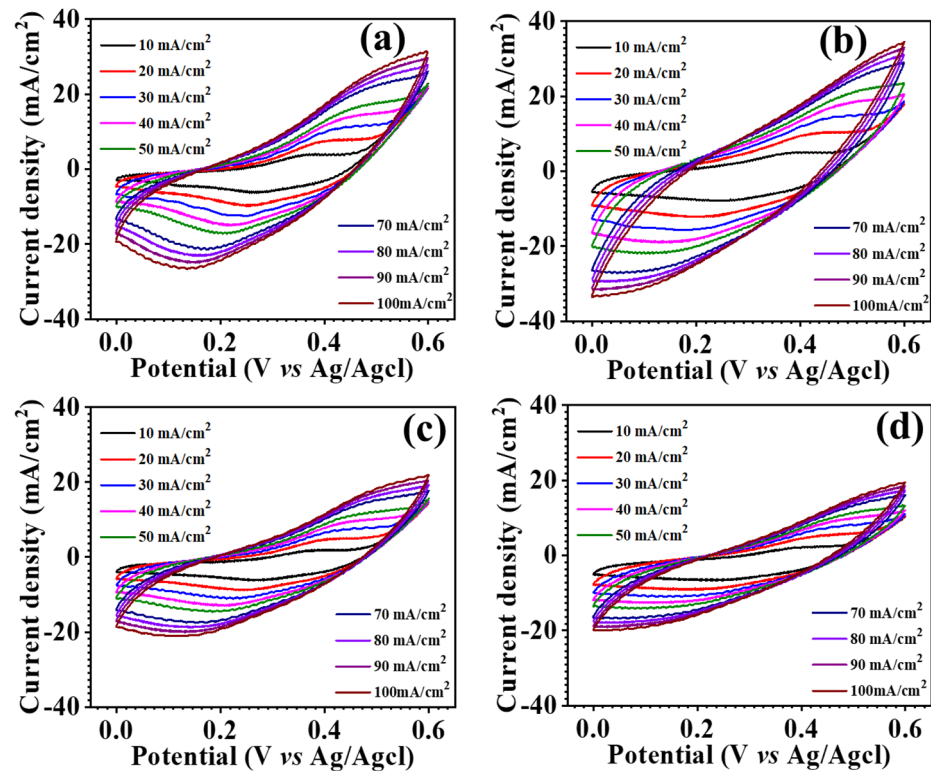


Figure 6. Cyclic voltammetry (CV) profile of  $\text{MnCo}_2\text{O}_4$  nanoparticles, MCO-0.2 MU (a), MCO-0.3 MU (b), MCO-0.4 MU (c), MCO-0.5 MU (d).

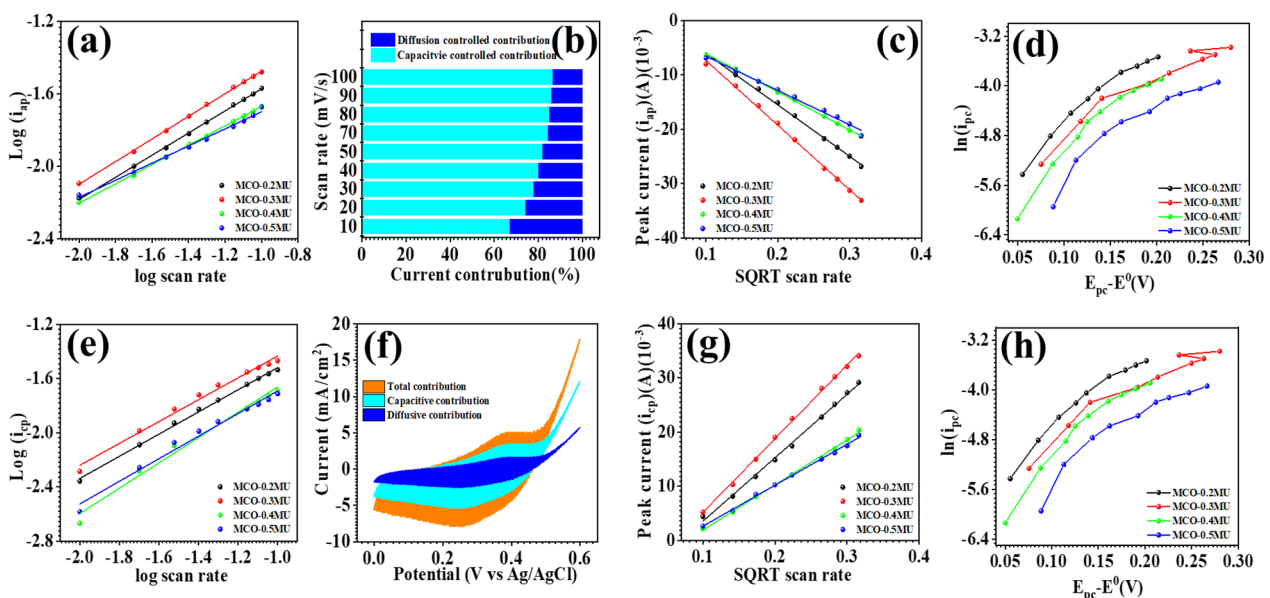


Figure 7.  $\text{Log } i_p$  vs.  $\text{log } v$  (a,e) of  $\text{MnCo}_2\text{O}_4$  electrodes prepared at different molar concentrations of urea, current contribution at 10 mV/s (b) of MCO-0.3 MU electrode,  $i_p$  vs.  $v^{0.5}$  (c,g) and  $\ln(i_{pc})$  vs.  $E_p - E^0$  (d,h) of  $\text{MnCo}_2\text{O}_4$  electrodes prepared at different molar concentrations of urea.

To determine the capacitive and diffusive current contributions, we evaluated the CV profiles at a constant potential and used Equation (2). The slope of the equation indicates the capacitive controlled contribution, while the intercept indicates the contribution controlled diffusion [34–38]. The MCO-0.3 MU electrode's  $b$  value (0.62) signifies contribution from both capacitive and diffusive processes. Figure 7b depict capacitive and diffusion

current contributions at different scan rates, with a single Figure 7f demonstrating these contributions for the MCO-0.3 MU electrode at 100 mV/s. The surface microstructure of MnCo<sub>2</sub>O<sub>4</sub> nanoparticles, which exhibits a flower-like morphology with petal structures made up of tiny particles arranged in nanowires, is attributed to the dominance of diffusive current contribution over capacitive current contribution for MCO-0.3 MU. This observation is consistent with the diffusion coefficient calculations that were calculated from Equation (3) [39,40], which show that the MCO-0.3 MU electrode has higher values for oxidation and reduction ( $4.31 \times 10^{-8}$  and  $5.9 \times 10^{-8}$  cm<sup>2</sup>/S) than other electrodes (values listed in Table 1).

$$i_p = 0.4463ACFn\sqrt{\frac{nFvD}{RT}} \quad (3)$$

$$i_p = 0.227nCAFk^0 \exp\left(-\left(\frac{\alpha nF}{RT}\right)(E_p - E^0)\right) \quad (4)$$

**Table 1.** Comparison of diffusion coefficient, C<sub>s</sub>, ED and PD MnCo<sub>2</sub>O<sub>4</sub> electrodes prepared at different molar concentrations of urea.

Sample Code	Diffusion Coefficient (cm <sup>2</sup> /S) 10 <sup>-8</sup>	Specific Capacitance (F g <sup>-1</sup> )
MCO-0.2 MU	3.07	251
MCO-0.3 MU	4.21	342
MCO-0.4 MU	1.71	161
MCO-0.5 MU	1.38	220

The electrochemical reaction process has been defined as quasireversible, reversible, or irreversible depending on the K<sup>0</sup> values that were calculated from Equation (4) [31,41,42]. The MCO-0.3 MU electrode's k<sup>0</sup> value ( $10.1 \times 10^{-5}$  and  $6.64 \times 10^{-5}$  cm/s) for charging and discharging suggests a quasireversible electrochemical reaction. The transfer coefficient, which represents the reaction process, is between 0 and 1 and was calculated using Equation (4) [43]. The difference in k<sup>0</sup> and transfer coefficient can be attributed to varying urea concentrations modifying the surface microstructure. As supported by the b value, higher diffusion coefficient, and dominance of diffusion current contribution at constant potential, a concentration of 0.3 M urea appears to be the optimized molar concentration, providing a large area under the CV profile and active sites for electrode-electrolyte interaction.

The GCD measurements for each nanostructure were utilized to look into the electrochemical performance of the electrode material, incorporating specific capacitance, energy density, and power density, as well as the asymmetric supercapacitor device. Figure 9b illustrates the GCD profiles of all electrodes in comparison, with the MCO-0.3 MU electrode having the largest charging and discharging intervals and GCD profile of all electrode, as shown in Figure 8a–d. The effect of raising the urea concentration on surface microstructures is shown in the GCE profiles. The surface microstructure of the MCO-0.2MU electrode was flower-like, with a compact petal-like shape. Its effect on electrode charging and discharging may be attributed to the limited area available for electrolyte-electrode interaction as a result of the compactness of the petal shape. Once the molecular concentration was tuned to 0.3 M, the flower's surface with free petals demonstrated favorable charging and discharging times. This might be because the free petals impart sufficient space for ion intercalations and deintercalation thus offering few challenges during the charging and discharging processes. By interconnecting the petals of the flower structures laterally with a urea concentration of 0.4 M, the surface morphology converted into a sheet-like structure. Because of the compactness of the sheet shape, this transition resulted in shorter charging and discharging times. Similarly, at 0.5 M urea concentration, a minor overgrowth of MnCo<sub>2</sub>O<sub>4</sub> nanoparticles on the sheet surface was detected, resulting in a modest increase in charging and discharging periods. The electrodes' specific capacitance, energy density, and

power density have been determined using the Formulas (5)–(7) [44–46] and are reported in Table 1.

$$C_s = \frac{I_d \cdot T_d}{A \cdot dV} \quad (5)$$

$$ED_s = \frac{C_s \cdot V^2}{7.2} \quad (6)$$

$$PD_s = \frac{3600 \cdot ED_s}{T_d} \quad (7)$$

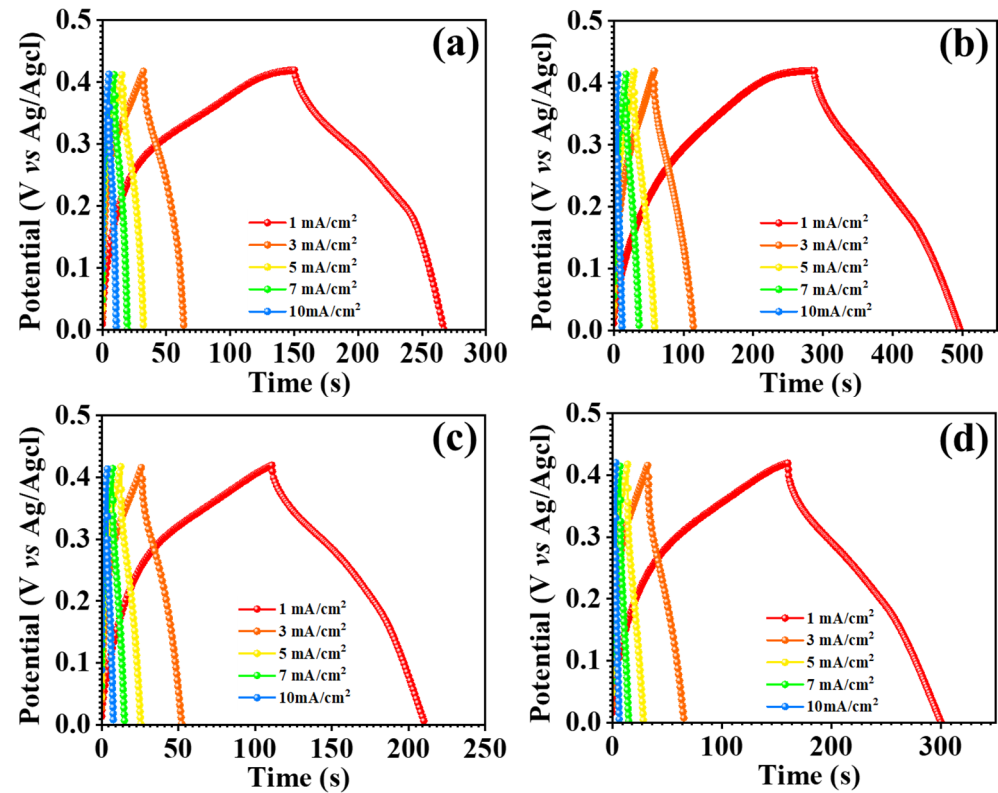


**Figure 8.** Galvanostatic charge discharge (GCD) profile of  $\text{MnCo}_2\text{O}_4$  nanoparticles, MCO-0.2MU (a), MCO-0.3MU (b), MCO-0.4MU (c), MCO-0.5MU (d).

The MCO-0.3MU electrode has a high energy storage capacity of  $342 \text{ F g}^{-1}$  at a current density of  $1 \text{ mA/cm}^2$  and an energy density of  $8.4 \text{ Wh/kg}$  at a power density of  $140 \text{ W/kg}$ . These remarkable MCO-0.3MU electrode findings were used to investigate the asymmetric supercapacitor using activated carbon as the other electrode and a  $2 \text{ M KOH}$  aqueous electrolyte. Electrochemical impedance spectroscopy (EIS) measurements were used to investigate the electrode transfer nature of all electrodes. Figure 9c depicts the  $\text{MnCo}_2\text{O}_4$  electrode's Nyquist plot, where the straight line in lower frequency areas shows electrolyte diffusion. The intercept on the x-axis indicates the series resistance ( $R_s$ ) at higher frequency areas, which occurs owing to the resistance of the electrode material, electrolyte, and electrode-electrolyte interface [46–50]. The charge transfer resistance ( $R_{ct}$ ) is represented by the semicircle diameter in EIS. Table 2 shows the  $R_s$  and  $R_{ct}$  values for all electrodes.  $R_s$  and  $R_{ct}$  values for the MCO-0.3 MU electrode were  $3.11 \Omega$  and  $1.76 \Omega$ , respectively. Smaller  $R_s$  and  $R_{ct}$  values might be attributed to the surface microstructure of the  $\text{MnCo}_2\text{O}_4$  electrode. The flower-like surface shape with free-space petals creates an obstacle-free surface, allowing for great energy storage capacity via simple electrode-electrolyte interaction.

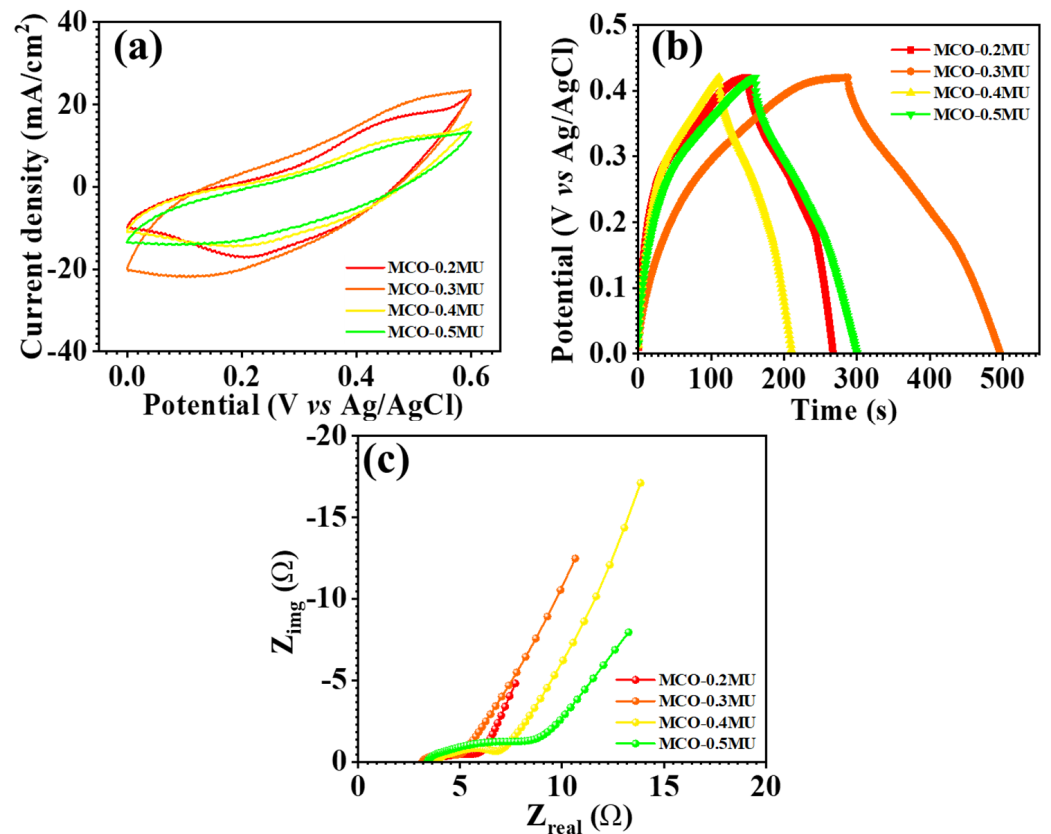


**Figure 9.** Comparative cyclic voltammetry CV (a), galvanostatic charge discharge GCD (b) and EIS (c) profile of  $\text{MnCo}_2\text{O}_4$  nanoparticles prepared at different molar concentrations of urea.

**Table 2.** Comparison of standard rate constant ( $k^0$ ), transfer coefficient ( $\alpha$ ), series resistance ( $R_s$ ), ED and charge transfer resistance ( $R_{ct}$ )  $\text{MnCo}_2\text{O}_4$  electrode prepared at different molar concentration of urea.

Sample Code	Standard Rate Constant $k^0$ (cm/S) $10^{-5}$	Transfer Coefficient ( $\alpha$ )	Series Resistance ( $R_s$ ) ( $\Omega$ )	Charge Transfer Resistance ( $R_{ct}$ ) ( $\Omega$ )
MCO-0.2 MU	5.18	0.32	3.61	2.24
MCO-0.3 MU	6.64	0.22	3.11	1.76
MCO-0.4 MU	2.71	0.35	3.83	2.95
MCO-0.5 MU	3.01	0.26	3.35	4.89

### 3.4. Device Electrochemical Study

The optimized electrode's practical application was studied through the fabrication of an asymmetric supercapacitor device by employing  $\text{MnCo}_2\text{O}_4$  (MCO) nanoparticles at 0.3 M urea concentration and an activated carbon (AC) electrode. The AC electrode and the MCO-0.3 MU electrode were constructed in an approach exactly as described in the electrode preparation section. The AC electrode and MCO-0.3 MU electrode were placed in a device, with filter paper acting as a separator between the two. A 2 M KOH electrolyte was used, and the device was firmly covered in paraffin paper to prevent electrolyte loss. The potential window of the MCO-0.3 MU // AC asymmetric supercapacitor (ASC) device was determined using cyclic voltammetry (CV) profiles. CV profiles of the MCO-0.3 MU // AC ASC device were acquired throughout several potential windows ranging from 1.0 V to 1.8 V. Up to 1.8 V, the potential rose steadily with the current, as seen in Figure 10b. The potential window of 1.8 V was set, and CV profiles were measured at various scan speeds (10–100 mV/s) as shown in Figure 10a. As the scan rate increased, so did the area beneath

the CV profile. Figure 10d shows the galvanostatic charge-discharge (GCD) profiles of the MCO-0.3 MU//AC ASC device measured at various potential windows to confirm its performance. Using a potential window of 1.8 V, GCD profiles were detected at scan speeds ranging from 4–10 mA/cm<sup>2</sup> as shown in Figure 10c. Equations (5)–(7) were used to determine the specific capacitance, energy density, and power density of the MCO-0.3 MU//AC ASC device. The device has a specific capacitance of 29 F g<sup>-1</sup> at 4 mA/cm<sup>2</sup>, energy density of 13 Wh/kg, and power density of 553 W/kg. Figure 10a shows the stability of MCO-0.3 MU//AC ASC for practical applications, and the MCO-0.3 MU//AC ASC device maintained 87% of its initial performance after 14,000 cycles. The interaction between electrodes and electrolytes was investigated using electrochemical impedance spectroscopy (EIS). Figure 10b shows EIS spectra of the MCO-0.3 MU//AC ASC device before and after stability testing revealed a rise in series resistance ( $R_s$ ) from 5.52  $\Omega$  to 6.91  $\Omega$ . The minor increase in series resistance might be attributable to surface alterations during lengthy stability testing. The mechanical flexibility of the ASC was tested by bending of the flexible ASC at 90°. Figure 11c,d shows the CV and GCD profile of the ASC at 0° and 90°. CV and GCD profiles show similar profiles and were overlapped with each other showing excellent flexibility. Overall, the study shows that electrodes made with a 0.3 M urea concentration have outstanding electrochemical performance, which is due to the distinctive surface shape of MnCo<sub>2</sub>O<sub>4</sub> nanoparticles. The ASC device made with MCO-0.3 MU and AC, has a remarkable energy density and power density, indicating that MnCo<sub>2</sub>O<sub>4</sub> nanoparticles synthesized at 0.3 M concentration have the potential to be useful electrodes for energy storage in supercapacitor applications.

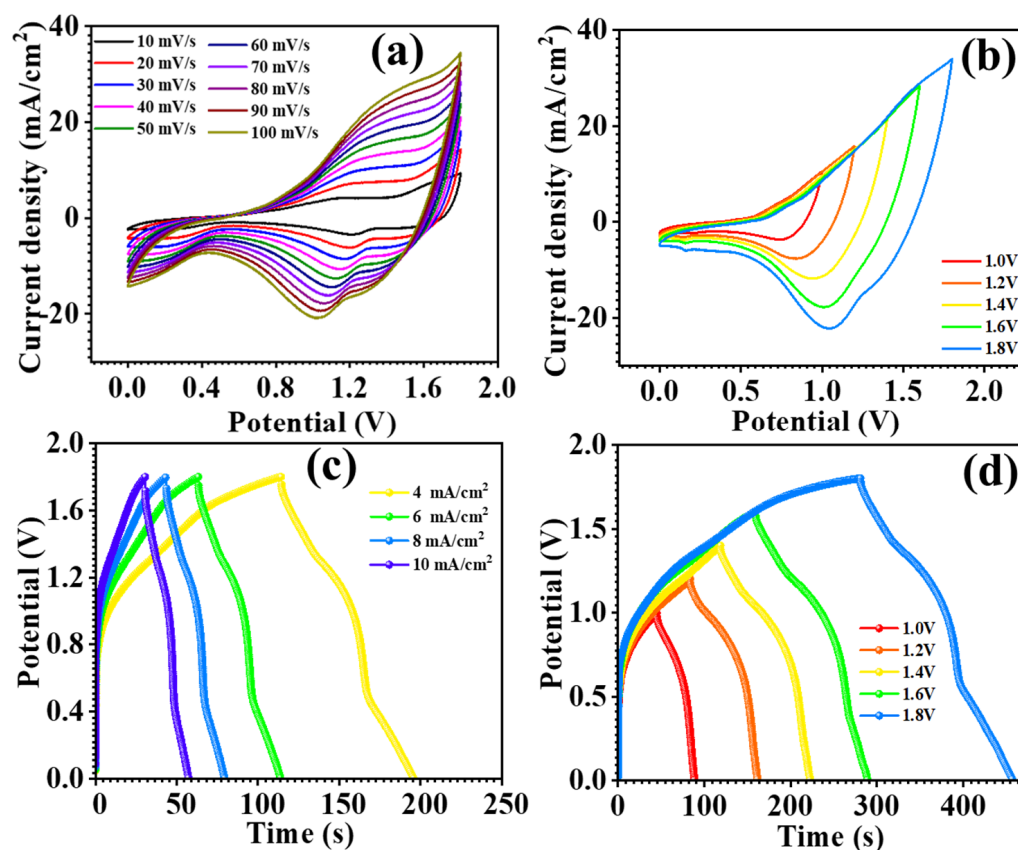
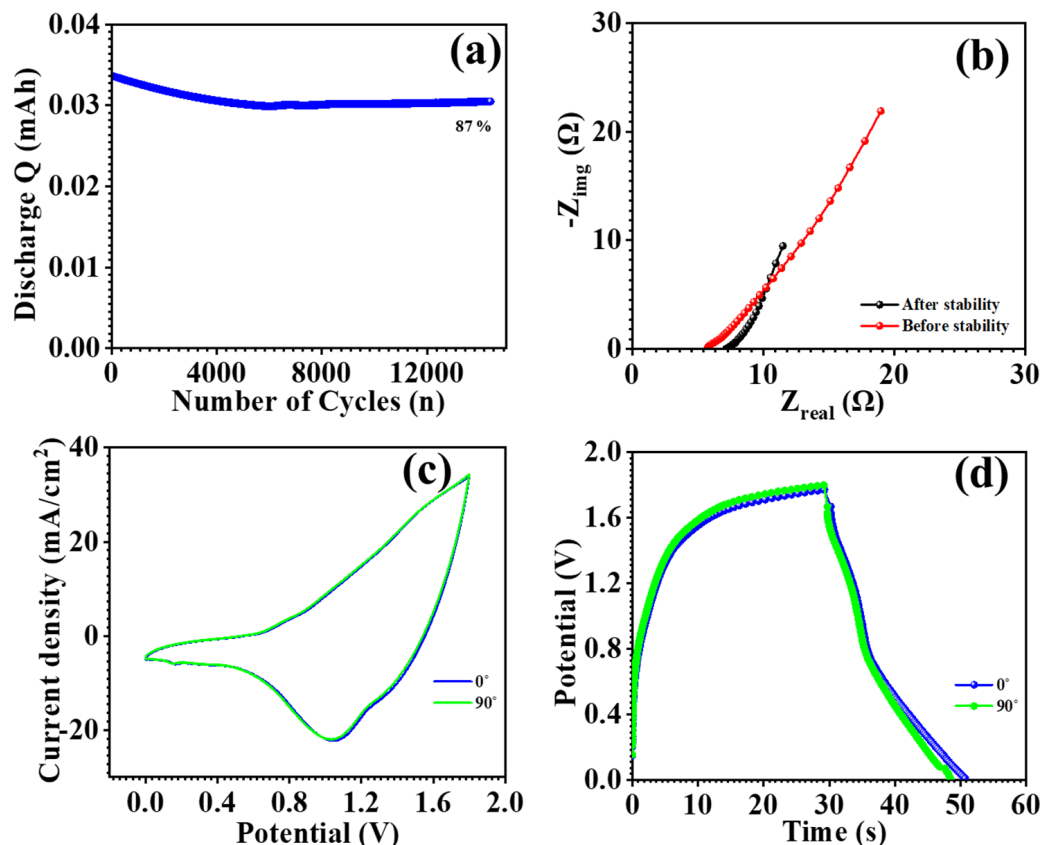


Figure 10. CV profile at different scan rates (a), CV profile at potential (b), GCD profile at different current densities (c), GCD profile at potential (d) of asymmetric supercapacitor (ASC).



**Figure 11.** GCD cyclic stability (a), EIS spectra (b) before and after cyclic stability, CV profile at  $0^\circ$  and  $90^\circ$  (c), GCD profile at  $0^\circ$  and  $90^\circ$ , (d) of asymmetric supercapacitor (ASC).

### 3.5. HER and OER Electrocatalysis Study

In order to study the electrocatalytic activity of the improved MCO-0.3 MU electrode, we used linear sweep voltammetry to measure the HER and OER. At a scan rate of 5 mV/s, the HER and OER LSV were operated in an aqueous electrolyte containing 1 M KOH. The three electrodes utilized in this experiment: a working electrode made of MCO-0.3 MU, a platinum electrode which served as counter electrode, and an Ag/AgCl electrode which served as a reference electrode. The potentials were converted into RHE from equation [51–53]. Figure 12a,d shows LSV plots for HER and OER, respectively. In comparison to RHE, the MCO-0.3 MU electrode displays overpotential of 358 mV and 1.46 V, respectively. The Tafel slopes were obtained from the equation seen in Figure 12b,e. The MCO-0.3 MU electrode's Tafel slope for HER is 356 mV/dec and for OER it was 187 mV/dec. Figure 10c,f show the EIS spectra of MCO-0.3 MU for HER and OER, through EIS analysis recorded in a 1 M KOH electrolyte at a scan rate of 5 mV/s over a frequency range of 0.1 Hz to 100 kHz. The electrocatalytic processes of HER and OER were investigated. For HER, the electrode's  $R_s$  value is 3.31  $\Omega$ , whereas for OER, it is 3.43  $\Omega$ . The nanowire in the floral surface shape of the  $\text{MnCo}_2\text{O}_4$  nanoparticle could be responsible for the remarkable overpotential and Tafel slope of the MCO-0.3 MU electrode for HER and OER. Extra electrolytic surface area, provided by access to the flower's available free space, demonstrates exceptional electrocatalytic activity. These outcomes indicate the potential that MCO-0.3 MU might be an attractive electrode material for water electrocatalysis.

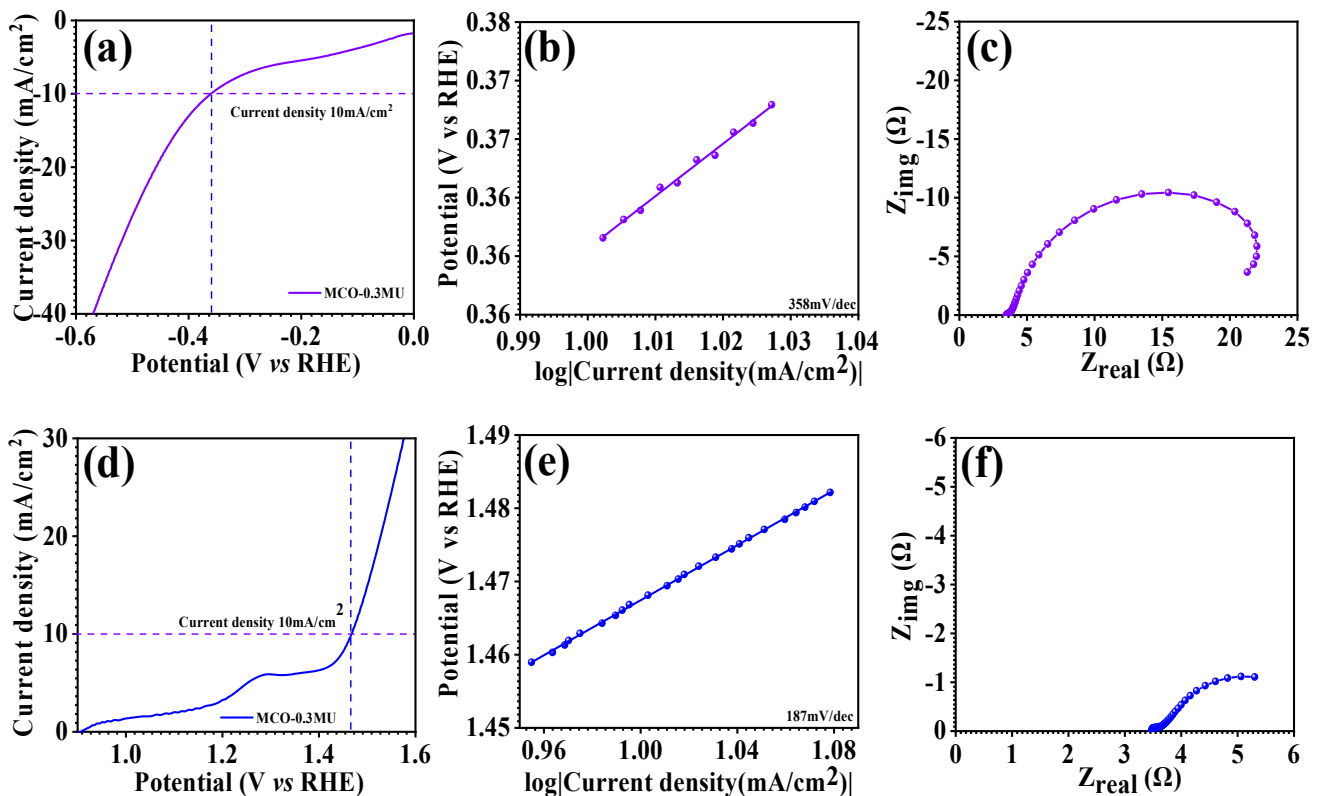


**Figure 12.** LSV profile (a), Tafel plot (b) and EIS spectra (c) of  $\text{MnCo}_2\text{O}_4$  (MCO-0.3 MU) electrode for HER, LSV profile (d), Tafel plot (e) and EIS spectra (f) of  $\text{MnCo}_2\text{O}_4$  (MCO-0.3 MU) electrode for OER.

#### 4. Conclusions

Varying the molar concentration of urea effectively changed the surface microstructure of  $\text{MnCo}_2\text{O}_4$  nanoparticles using a hydrothermal method. The surface modifications significantly affected the electrode's chemical performance. In a three-electrode arrangement, the  $\text{MnCo}_2\text{O}_4$  nanoparticles prepared at a 0.3 M urea concentration displayed a flower-like microstructure. Furthermore, the  $\text{MnCo}_2\text{O}_4$  electrode exhibited a superior specific capacitance of  $342 \text{ F g}^{-1}$  and an energy density of  $8.4 \text{ Wh/kg}$  at a power density of  $140 \text{ W/kg}$ . Studies into electrochemical impedance revealed a charge transfer resistance of  $1.79 \Omega$  and a series resistance of  $3.11 \Omega$ .  $\text{MnCo}_2\text{O}_4$  nanoparticles and activated carbon electrodes were used to develop asymmetric supercapacitors (ASCs). The ASCs demonstrated a remarkable  $29 \text{ F g}^{-1}$  specific capacitance at  $4 \text{ mA/cm}^2$  current density and  $13 \text{ Wh/kg}$  energy density at  $553 \text{ W/kg}$  power density. According to cyclic stability testing, the ASCs retained 87% of their capacity across 14K GCD cycles. EIS measurements of the ASCs found a series resistance of  $5.54 \Omega$  before cyclic stability and  $7.01 \Omega$  after cyclic stability. Electrocatalysis investigations revealed overpotential of  $358 \text{ mV}$  and  $1.48 \text{ V}$  for HER and OER, respectively, with Tafel slopes of  $356 \text{ mV/dec}$  and  $187 \text{ mV/dec}$ . Series resistances for both the HER and OER from EIS experiments were  $3.48 \Omega$ . Together with the stability of ASC devices, the remarkable specific capacitance, energy density, and power density of ASCs as well as the exceptional electrocatalytic HER and OER performance of  $\text{MnCo}_2\text{O}_4$  nanoparticles show potential for a wide range of applications.

**Author Contributions:** Methodology, M.A.Y.; Formal analysis, A.M.T.; Data curation, S.A.B. and V.K.; Funding acquisition, validation and write review and editing, D.-K.S. All authors have read and agreed to the published version of the manuscript.

**Funding:** This work was supported by the Technology Innovation Program (20010170) funded by the Ministry of Trade, Industry & Energy (MOTIE, Korea).

**Institutional Review Board Statement:** Not applicable.

**Informed Consent Statement:** Not applicable.

**Data Availability Statement:** Data are contained within the article.

**Conflicts of Interest:** The authors declare no conflicts of interest.

## References

1. Rendale, S.S.; Bhat, T.S.; Patil, P.S. MnCo<sub>2</sub>O<sub>4</sub> nanomaterials based electrodes for supercapacitors. *Inorg. Chem. Commun.* **2022**, *145*, 109945. [[CrossRef](#)]
2. Kumari, K.; Joy, A.; Saren, P.; Acharya, S.; De, S.; Behera, A.K.; Mahanti, B.; Nayak, G.C. Synthesis of highly porous hybrid nanocomposite of hemp derived carbon nanosheet/carbon nanotube/manganese cobalt oxide for asymmetric supercapacitor. *Mater. Chem. Phys.* **2024**, *313*, 128677. [[CrossRef](#)]
3. Chomkhuntod, P.; Phonsuksawang, P.; Waehayee, A.; Ngamchuea, K.; Iamprasertkun, P.; Maensiri, S.; Ruangvittayanon, A.; Siritanon, T. Effect of solvent-dependent morphology on charge storage mechanism of NiCo<sub>2</sub>O<sub>4</sub> for aqueous supercapacitors. *J. Energy Storage* **2024**, *86*, 111303. [[CrossRef](#)]
4. Himasree, P.; Durga, I.K.; Krishna, T.N.V.; Rao, S.S.; Gopi, C.V.V.M.; Revathi, S.; Prabakar, K.; Kim, H.J. One-step hydrothermal synthesis of CuS@MnS on Ni foam for high performance supercapacitor electrode material. *Electrochim. Acta* **2019**, *305*, 467–473. [[CrossRef](#)]
5. Zardkhouhoui, A.M.; Davarani, S.S.H. Ultrahigh energy density supercapacitors based on facile synthesized Ni<sub>2</sub>CoOH-rGO/NF hybrid electrodes. *J. Alloys Compd.* **2018**, *769*, 922–931. [[CrossRef](#)]
6. Mu, J.; Li, C.; Zhang, J.; Song, X.; Chen, S.; Xu, F. Efficient conversion of lignin waste and self-assembly synthesis of C@MnCo<sub>2</sub>O<sub>4</sub> for asymmetric supercapacitors with high energy density. *Green Energy Environ.* **2023**, *8*, 1479–1487. [[CrossRef](#)]
7. Lokhande, C.D.; Dubal, D.P.; Joo, O.S. Metal oxide thin film based supercapacitors. *Curr. Appl. Phys.* **2011**, *11*, 255–270. [[CrossRef](#)]
8. Guan, D.; Wang, B.; Zhang, J.; Shi, R.; Jiao, K.; Li, L.; Wang, Y.; Xie, B.; Zhang, Q.; Yu, J.; et al. Hydrogen society: From present to future. *Energy Environ. Sci.* **2023**, *16*, 4926–4943. [[CrossRef](#)]
9. Hussain, S.; Vikraman, D.; Sheikh, Z.A.; Mehran, M.T.; Shahzad, F.; Batoor, K.M.; Kim, H.S.; Kim, D.K.; Ali, M.; Jung, J. WS<sub>2</sub>-embedded MXene/GO hybrid nanosheets as electrodes for asymmetric supercapacitors and hydrogen evolution reactions. *Chem. Eng. J.* **2023**, *452*, 139523. [[CrossRef](#)]
10. Mohite, S.V.; Kim, S.; Bae, J.; Jeong, H.J.; Kim, T.W.; Choi, J.; Kim, Y. Defects Healing of the ZnO Surface by Filling with Au Atom Catalysts for Efficient Photocatalytic H<sub>2</sub> Production. *Small* **2024**, *20*, e2304393. [[CrossRef](#)] [[PubMed](#)]
11. Rebekah, A.; Amir, H.; Viswanathan, C.; Ponpandian, N. Enhanced bifunctional aspects of oxygen vacancy rich cation substituted MnCo<sub>2</sub>O<sub>4</sub> intercalated with g-C<sub>3</sub>N<sub>4</sub> as an oxygen evolution and supercapacitor electrode. *Int. J. Hydrog. Energy* **2023**, *48*, 6384–6398. [[CrossRef](#)]
12. Dey, N.; Sharma, P.; Ray, S.K.; Guha, P.K. Flexible micro-supercapacitors with organic gel electrolytes based on screen-printable CuO-ink. *Electrochim. Acta* **2024**, *475*, 143634. [[CrossRef](#)]
13. Karade, S.S.; Banerjee, K.; Majumder, S.; Sankapal, B.R. Novel application of non-aqueous chemical bath deposited Sb<sub>2</sub>S<sub>3</sub> thin films as supercapacitive electrode. *Int. J. Hydrog. Energy* **2016**, *41*, 21278–21285. [[CrossRef](#)]
14. Shukla, P.S.; Agrawal, A.; Gaur, A.; Varma, G.D. Synthesis of mesoporous Zn-doped MnCo<sub>2</sub>O<sub>4</sub> nanoparticles for high-energy density solid-state asymmetric supercapacitor. *J. Energy Storage* **2023**, *73*, 109229. [[CrossRef](#)]
15. Naik, P.S.; Redekar, R.S.; Kamble, J.V.; Patil, K.V.; Tayade, S.N.; Patil, V.L.; Tarwal, N.L.; Karanjakar, M.M.; Kamble, P.D. Binderless synthesis of hierarchical, marigold flower-like NiCo<sub>2</sub>O<sub>4</sub> films for high-performance symmetric supercapacitor. *J. Energy Storage* **2024**, *86*, 111302. [[CrossRef](#)]
16. Krittayavathananon, A.; Pettong, T.; Kidkhunthod, P.; Sawangphruk, M. Insight into the charge storage mechanism and capacity retention fading of MnCo<sub>2</sub>O<sub>4</sub> used as supercapacitor electrodes. *Electrochim. Acta* **2017**, *258*, 1008–1015. [[CrossRef](#)]
17. Pallavolu, M.R.; Thomas, S.A.; Cherusseri, J.; Al-Asbahi, B.A.; Das, H.T.; Adem, S.; Joo, S.W. Scalable synthesis of binder-free hierarchical MnCo<sub>2</sub>O<sub>4</sub> nanospikes/Ni(OH)<sub>2</sub> nanosheets composite electrodes for high-capacity supercapacitors. *J. Energy Storage* **2023**, *73*, 108999. [[CrossRef](#)]
18. Mkhali, I.A.; Ismail, A.A.; Hussein, M.A.; Thomali, R.H.M.A. Nanoheterojunctions MnCo<sub>2</sub>O<sub>4</sub> nanoparticles anchored on mesoporous TiO<sub>2</sub> networks for superior photocatalytic ability. *Mater. Res. Bull.* **2023**, *167*, 112439. [[CrossRef](#)]
19. Kour, S.; Kour, P.; Sharma, A.L. Self-assembled carbon wrapped manganese cobaltite nano-composite with promising electrochemical performance for symmetric and asymmetric supercapacitor device. *J. Energy Storage* **2023**, *68*, 107813. [[CrossRef](#)]
20. Azizi, S.; Seifi, M.; Moghadam, M.T.T.; Jamali, F.; Salarizadeh, P.; Askari, M.B. MnCo<sub>2</sub>O<sub>4</sub>/activated carbon wheat husk (ACWH) as a novel electrode material for electrochemical capacitors. *Diam. Relat. Mater.* **2023**, *137*, 110061. [[CrossRef](#)]
21. Kumar, S.A.; Sindhuja, V.; Gowdhaman, A.; Balaji, C.; Ramesh, R.; Anbarasan, P.M. Construction of vertically aligned MnCo<sub>2</sub>O<sub>4</sub> needles and Bi<sub>2</sub>WO<sub>6</sub> globules as optimal electrode materials for hybrid supercapacitor. *Electrochim. Acta* **2023**, *459*, 142545. [[CrossRef](#)]
22. Rendale, S.S.; Beknalkar, S.A.; Teli, A.M.; Shin, J.C.; Bhat, T.S. Hydrothermally synthesized aster flowers of MnCo<sub>2</sub>O<sub>4</sub> for development of high-performance asymmetric coin cell supercapacitor. *J. Electroanal. Chem.* **2023**, *932*, 117253. [[CrossRef](#)]
23. Silambarasan, S.; Maiyalagan, T. Nitrogen-doped porous carbon coated on MnCo<sub>2</sub>O<sub>4</sub> nanospheres as electrode materials for high-performance asymmetric supercapacitors. *Mater. Today Chem.* **2023**, *27*, 101350. [[CrossRef](#)]

24. Auti, P.S.; Yewale, M.A.; Kadam, R.A.; Kumar, R.; Nakate, U.T.; Teli, A.M.; Jadhavar, A.A.; Kumar, V.; Warule, S.S.; Shin, D.K. Materials Science & Engineering B Hydrothermally synthesized  $\text{MnCo}_2\text{O}_4$  nanoparticles for advanced energy storage applications. *Mater. Sci. Eng. B* **2024**, *301*, 117198. [[CrossRef](#)]
25. Hong, J.; Lee, Y.W.; Ahn, D.; Pak, S.; Lee, J.; Jang, A.R.; Lee, S.; Hou, B.; Cho, Y.; Morris, S.M.; et al. Highly stable 3D porous heterostructures with hierarchically-coordinated octahedral transition metals for enhanced performance supercapacitors. *Nano Energy* **2017**, *39*, 337–345. [[CrossRef](#)]
26. Kotalgi, K.; Kanojiya, A.; Tisekar, A.; Salame, P.H. Electronic transport and electrochemical performance of  $\text{MnCo}_2\text{O}_4$  synthesized using the microwave-assisted sonochemical method for potential supercapacitor application. *Chem. Phys. Lett.* **2022**, *800*, 139660. [[CrossRef](#)]
27. Wang, M.; Chen, K.; Liu, J.; He, Q.; Li, G.; Li, F. Efficiently enhancing electrocatalytic activity of  $\alpha\text{-MnO}_2$  nanorods/N-doped ketjenblack carbon for oxygen reduction reaction and oxygen evolution reaction using facile regulated hydrothermal treatment. *Catalysts* **2018**, *8*, 138. [[CrossRef](#)]
28. Dong, S.; Wang, L.; Liu, Y.; Li, X.; Chen, G.; Cao, Z.; Zhang, Y. HP- $\text{MnCo}_2\text{O}_4/\text{C}$  nanomaterials synthesized by Co Mn metal organic framework supported with the pyridine-3,5-dicarboxylate ligand for anode in lithium-ion batteries. *Ionics* **2022**, *28*, 1667–1677. [[CrossRef](#)]
29. Nagamuthu, S.; Vijayakumar, S.; Lee, S.H.; Ryu, K.S. Hybrid supercapacitor devices based on  $\text{MnCo}_2\text{O}_4$  as the positive electrode and  $\text{FeMn}_2\text{O}_4$  as the negative electrode. *Appl. Surf. Sci.* **2016**, *390*, 202–208. [[CrossRef](#)]
30. Naresh, B.; Kuchi, C.; Rajasekhar, D.; Reddy, P.S. Solvothermal synthesis of  $\text{MnCo}_2\text{O}_4$  microspheres for high-performance electrochemical supercapacitors. *Colloids Surf. A Physicochem. Eng. Asp.* **2022**, *640*, 128443. [[CrossRef](#)]
31. Lindström, H.; Södergren, S.; Solbrand, A.; Rensmo, H.; Hjelm, J.; Hagfeldt, A.; Lindquist, S.E.  $\text{Li}^+$  ion insertion in  $\text{TiO}_2$  (anatase). 1. Chronoamperometry on CVD films and nanoporous films. *J. Phys. Chem. B* **1997**, *101*, 7710–7716. [[CrossRef](#)]
32. Jadhavar, A.A.; Shelke, N.T.; Yewale, M.A.; Kadam, R.A.; Kadam, S.L.; Shin, D.K. Hydrothermal Synthesis of Cobalt Vanadium Oxide ( $\text{Co}_3\text{V}_2\text{O}_8$ ) Hexagonal Disc for High-Performance Supercapacitors. *Surf. Interfaces* **2023**, *43*, 103519. [[CrossRef](#)]
33. Yewale, M.A.; Kumar, V.; Kadam, R.A.; Kharade, R.B.; Teli, A.M.; Beknalkar, S.A.; Dhas, S.D.; Nakate, U.T.; Shin, D.K. Wrapped nanochain microstructures of  $\text{Ni}_3\text{V}_2\text{O}_8$  nanoparticles for supercapacitor applications using the hydrothermal method. *J. Energy Storage* **2023**, *73*, 109005. [[CrossRef](#)]
34. Liu, T.-C.; Pell, W.G.; Conway, B.E.; Roberson, S.L. Behavior of Molybdenum Nitrides as Materials for Electrochemical Capacitors: Comparison with Ruthenium Oxide. *J. Electrochem. Soc.* **1998**, *145*, 1882–1888. [[CrossRef](#)]
35. Zhang, H.; Wang, L.; Xing, X.; Zhao, S.; Wang, K.; Liu, S. High-Energy-Density Supercapacitors Based on High-Areal-Specific-Capacity  $\text{Ti}_3\text{C}_2\text{T}_x$  and a Redox-Active Organic-Molecule Hybrid Electrode. *Adv. Funct. Mater.* **2022**, *32*, 2208403. [[CrossRef](#)]
36. Zhang, Y.S.; Lu, C.; Hu, Y.X.; Zhang, B.M.; Li, J.; Tian, C.Y.; Zhang, D.T.; Kong, L.B.; Liu, M.C. Assemble from 0D to 3D: Anchored 0D molybdenum carbide on 3D octahedral amorphous carbon with excellent capacitive properties. *J. Mater. Sci.* **2020**, *55*, 15562–15573. [[CrossRef](#)]
37. Wang, J.; Zhao, H.; Xu, L.; Yang, Y.; He, G.; Du, Y. Three-Electron Redox Enabled Dithiocarboxylate Electrode for Superior Lithium Storage Performance. *ACS Appl. Mater. Interfaces* **2018**, *10*, 35469–35476. [[CrossRef](#)]
38. Shanmugavadeivel, M.; Dhayabaran, V.V.; Subramanian, M. Fabrication of high energy and high power density supercapacitor based on  $\text{MnCo}_2\text{O}_4$  nanomaterial. *J. Phys. Chem. Solids* **2019**, *133*, 15–20. [[CrossRef](#)]
39. Wang, B.; Aoki, K.J.; Chen, J.; Nishiumi, T. Slow scan voltammetry for diffusion-controlled currents in sodium alginate solutions. *J. Electroanal. Chem.* **2013**, *700*, 60–64. [[CrossRef](#)]
40. Teli, A.M.; Bhat, T.S.; Beknalkar, S.A.; Mane, S.M.; Chaudhary, L.S.; Patil, D.S.; Pawar, S.A.; Efstathiadis, H.; Shin, J.C. Bismuth manganese oxide based electrodes for asymmetric coin cell supercapacitor. *Chem. Eng. J.* **2022**, *430*, 133138. [[CrossRef](#)]
41. Rogers, J.A.; Maznev, A.A.; Banet, M.J.; Nelson, K.A. Optical Generation and Characterization of Acoustic Waves in Thin Films: Fundamentals and Applications. *Annu. Rev. Mater. Sci.* **2000**, *30*, 117–157. [[CrossRef](#)]
42. Matsuda, H.; Ayabe, Y. Zur Theorie der Randles-Sevčičschen Kathodenstrahl-Polarographie. *Z. Elektrochem. Ber. Bunsenges. Phys. Chem.* **1955**, *59*, 494–503. [[CrossRef](#)]
43. Frenzel, N.; Hartley, J.; Frisch, G. Voltammetric and spectroscopic study of ferrocene and hexacyanoferrate and the suitability of their redox couples as internal standards in ionic liquids. *Phys. Chem. Chem. Phys.* **2017**, *19*, 28841–28852. [[CrossRef](#)] [[PubMed](#)]
44. Anjana, P.M.; Kumar, S.R.S.; Rakhi, R.B.  $\text{MnCo}_2\text{O}_4$  nanoneedles self-organized microstructures for supercapacitors. *Mater. Today Commun.* **2021**, *28*, 102720. [[CrossRef](#)]
45. Panah, T.S.; Shirvani, M.; Davarani, S.S.H. Bimetallic  $\text{NiCo}_2\text{Se}_4/\text{Fe}_2\text{CoSe}_4$  chrysanthemum flowers assembled by nanosheets: An efficient electrode material for hybrid supercapacitor applications. *J. Alloys Compd.* **2024**, *978*, 173496. [[CrossRef](#)]
46. Wang, T.; Guo, J.; Guo, Y.; Feng, J.; Wu, D. Nitrogen-Doped Carbon Derived from Deep Eutectic Solvent as a High-Performance Supercapacitor. *ACS Appl. Energy Mater.* **2021**, *4*, 2190–2200. [[CrossRef](#)]
47. Zhao, X.; Zhang, M.; Li, H.; Pan, W.; Luo, Z.; Sun, X. Smart construction of  $\text{MnCo}_2\text{O}_4$  microspheres with multiple interiors: Morphological evolution and structure-performance relationship for supercapacitor electrodes. *Appl. Surf. Sci.* **2022**, *600*, 154062. [[CrossRef](#)]
48. Xia, J.; Zhang, L.; Xuan, S.; Ni, Y.; Zhang, L. A self-templating scheme for the synthesis of  $\text{NiCo}_2\text{Se}_4$  and BiSe hollow microspheres for high-energy density asymmetric supercapacitors. *CrystEngComm* **2022**, *24*, 2159–2170. [[CrossRef](#)]

49. Song, K.; Li, W.; Xin, J.; Zheng, Y.; Chen, X.; Yang, R.; Lv, W.; Li, Q. Hierarchical porous heterostructured  $\text{Co}(\text{OH})_2/\text{CoSe}_2$  nanoarray: A controllable design electrode for advanced asymmetrical supercapacitors. *Chem. Eng. J.* **2021**, *419*, 129435. [[CrossRef](#)]
50. Baji, D.S.; Jadhav, H.S.; Nair, S.V.; Rai, A.K. Porous  $\text{MnCo}_2\text{O}_4$  as superior anode material over  $\text{MnCo}_2\text{O}_4$  nanoparticles for rechargeable lithium ion batteries. *J. Solid State Chem.* **2018**, *262*, 191–198. [[CrossRef](#)]
51. Mishra, R.K.; Kumar, V.; Trung, L.G.; Choi, G.J.; Ryu, J.W.; Kumar, P.; Bhardwaj, R.; Lee, S.H.; Gwag, J.S. Bifunctionality of  $\text{MoS}_2$  nanolayer catalyst for water-splitting reactions of hydrogen and oxygen. *Mater. Lett.* **2023**, *338*, 134026. [[CrossRef](#)]
52. Mishra, R.K.; Choi, G.J.; Ryu, J.W.; Singh, J.; Kumar, S.; Mishra, Y.K.; Lee, S.H.; Gwag, J.S. Unveiling the Transformative Potential of SWCNT/ $\text{In}_2\text{O}_3$  Heterostructures as High-Performance Catalysts for Overall Water Splitting. *Energy Fuels* **2023**, *37*, 19785–19800. [[CrossRef](#)]
53. Yewale, M.A.; Jadhvar, A.A.; Kharade, R.B.; Kadam, R.A.; Kumar, V.; Nakate, U.T.; Shelke, P.B.; Bobade, D.H.; Teli, A.M.; Dhas, S.D.; et al. Hydrothermally synthesized  $\text{Ni}_3\text{V}_2\text{O}_8$  nanoparticles with horny surfaces for HER and supercapacitor application. *Mater. Lett.* **2023**, *338*, 134033. [[CrossRef](#)]

**Disclaimer/Publisher’s Note:** The statements, opinions and data contained in all publications are solely those of the individual author(s) and contributor(s) and not of MDPI and/or the editor(s). MDPI and/or the editor(s) disclaim responsibility for any injury to people or property resulting from any ideas, methods, instructions or products referred to in the content.